

Characterization and correction of diffusion gradient-induced eddy currents in second-order motion-compensated echo-planar and spiral cardiac DTI

Robbert J. H. van Gorkum¹  | Christian Guenther¹  | Andreas Koethe^{1,2} |
Christian T. Stoeck^{1,3}  | Sebastian Kozerke¹  

¹Institute for Biomedical Engineering, University and ETH Zurich, Zurich, Switzerland

²Center for Proton Therapy, Paul Scherrer Institute, Villigen, Switzerland

³Division of Surgical Research, University Hospital Zurich, University Zurich, Zurich, Switzerland

Correspondence

Sebastian Kozerke, Institute for Biomedical Engineering, University and ETH Zurich, Gloriastrasse 35, 8092 Zurich, Switzerland.
Email: kozerke@biomed.ee.ethz.ch

Funding Information

Funding provided by the Swiss National Science Foundation (SNSF), grants CR23I3_166485 and PZ00P2_174144

Purpose: Very high gradient amplitudes played out over extended time intervals as required for second-order motion-compensated cardiac DTI may violate the assumption of a linear time-invariant gradient system model. The aim of this work was to characterize diffusion gradient-related system nonlinearity and propose a correction approach for echo-planar and spiral spin-echo motion-compensated cardiac DTI.

Methods: Diffusion gradient-induced eddy currents of 9 diffusion directions were characterized at b values of 150 s/mm^2 and 450 s/mm^2 for a 1.5 Tesla system and used to correct phantom, ex vivo, and in vivo motion-compensated cardiac DTI data acquired with echo-planar and spiral trajectories. Predicted trajectories were calculated using gradient impulse response function and diffusion gradient strength- and direction-dependent zeroth- and first-order eddy current responses. A reconstruction method was implemented using the predicted k -space trajectories to additionally include off-resonances and concomitant fields. Resulting images were compared to a reference reconstruction omitting diffusion gradient-induced eddy current correction.

Results: Diffusion gradient-induced eddy currents exhibited nonlinear effects when scaling up the gradient amplitude and could not be described by a 3D basis alone. This indicates that a gradient impulse response function does not suffice to describe diffusion gradient-induced eddy currents. Zeroth- and first-order diffusion gradient-induced eddy current effects of up to -1.7 rad and -16 to $+12 \text{ rad/m}$, respectively, were identified. Zeroth- and first-order diffusion gradient-induced eddy current correction yielded improved image quality upon image reconstruction.

Conclusion: The proposed approach offers correction of diffusion gradient-induced zeroth- and first-order eddy currents, reducing image distortions to promote improvements of second-order motion-compensated spin-echo cardiac DTI.

KEYWORDS

cardiac DTI, eddy currents, EPI, GIRF, image reconstruction, spiral imaging

This is an open access article under the terms of the Creative Commons Attribution-NonCommercial-NoDerivs License, which permits use and distribution in any medium, provided the original work is properly cited, the use is non-commercial and no modifications or adaptations are made.

© 2022 The Authors. *Magnetic Resonance in Medicine* published by Wiley Periodicals LLC on behalf of International Society for Magnetic Resonance in Medicine.

1 | INTRODUCTION

MR cardiac DTI (cDTI) offers noninvasive characterization of myofiber architecture, allowing the study of cardiac diseases and their effects on myofiber aggregates.¹⁻⁷ A key limitation of cDTI sequences is the relatively low SNR^{8,9} caused by the use of stimulated-echo acquisition^{10,11} or by an increased TE when using second-order motion-compensated (MC) diffusion gradients in spin-echo (SE) cDTI.^{8,9,12-14}

To increase SNR in MC-SE cDTI, powerful gradient systems need to be employed to reduce TE, which in turn can cause significant eddy current-induced distortions.¹⁵ Although readouts such as spirals are an appealing method to further reduce TE in cDTI,^{16,17} effects such as field inhomogeneities, gradient imperfections, and eddy currents can cause image distortions and intravoxel signal dephasing.^{15,18-20} In addition, T_2^* decay modulates the point spread function.^{16,19} Data reconstruction steps for spiral and EPI trajectories have been proposed to address off-resonances,^{18,21,22} trajectory-induced eddy currents,^{23,24} and concomitant fields.^{25,26} Eddy current effects of first-order MC-SE cDTI have previously been investigated in a phantom setting.¹⁵

Characterization and correction of eddy currents originating from diffusion-encoding gradients are challenging to perform in cDTI for several reasons. First, dedicated hardware approaches such as concurrent field monitoring²⁷ are impractical because they are sensitive to cardiac and respiratory motion.²⁸ Second, although phantom-based methodologies for gradient impulse response function (GIRF) characterization can be employed, they only allow the characterization of a frequency band between 0.1 and 10 kHz.^{23,29,30} Second-order diffusion-encoding gradients exhibit the strongest frequency responses around 25 to 50 Hz, which lie outside this sensitivity range. Finally, the use of a GIRF assumes the system to be linear and time-invariant. Although gradient amplifiers behave predominantly linear, non-linear responses or time-dependent effects³¹ violate this assumption.

The aim of the study at hand was to characterize and correct diffusion gradient-induced eddy currents in second-order MC-SE cDTI. A staged approach to analyzing and correcting eddy current effects induced by diffusion gradients is proposed. A study using a phantom and an ex vivo heart was performed to demonstrate the correction of diffusion gradient-induced eddy currents along with correction for off-resonances and trajectory-induced concomitant fields in echo-planar and spiral MC-SE cDTI. In vivo cDTI measurements on volunteers using both readout strategies were performed to

demonstrate the feasibility of the proposed correction approaches.

2 | THEORY

2.1 | Signal model

Given a gradient impulse response $h_{mn}(t)$ and input current $i_n(t)$, the gradient output $g_m(t)$ is obtained as

$$g_m(t) = \sum_n \int_0^t h_{mn}(t - \tau) i_n(\tau) d\tau, \quad (1)$$

with input channel $n = \{x, y, z\}$, output channel $m = \{1, x, y, z\}$, assuming zeroth- and first-order gradient terms; t defines the time with respect to the center of the excitation pulse. The gradient self-terms are defined by $m = n$, and gradient cross-terms by $m \neq n$. Upon Fourier transform of Equation 1, leading to $G_m(\nu) = \sum_n H_{mn}(\nu) I_n(\nu)$, with ν the frequency in Hz, the gradient transfer function $H_{mn}(\nu)$ is defined, which is also frequently referred to as GIRF or gradient-modulation transfer function.^{29,30}

$$H_{mn}(\nu) = \frac{G_m(\nu)}{I_n(\nu)}. \quad (2)$$

We can now define the simplified MR k -space signal $d(t, \vec{b})$ while excluding relaxation effects according to

$$d_c(t, \vec{b}) = \int M_{xy}(\vec{r}, t) \cdot C_c(\vec{r}) \cdot e^{i\vec{k}(t) \cdot \vec{r}'} \cdot e^{i\gamma \delta B_0(\vec{r}) t} \cdot e^{-\vec{b}^T \overline{\overline{D}}(\vec{r}) \vec{b}} d^3 r + \eta, \quad (3)$$

with $M_{xy}(\vec{r}, t)$ the transverse magnetization at time t and spatial locations $\vec{r} = [x, y, z]^T$, $\vec{r}' = [1 \ \vec{r}]^T = [1 \ x \ y \ z]^T$, $C_c(\vec{r})$ spatial coil sensitivities for coil c , i the imaginary number, γ the gyromagnetic ratio, $\delta B_0(\vec{r})$ spatially dependent off-resonances, \vec{b} the diffusion gradient vector with magnitude $\sqrt{b \text{ value}}$, $\overline{\overline{D}}(\vec{r})$ the spatially dependent diffusion tensor, T the transpose operator, and η complex-valued Gaussian noise. The k -space vector $\vec{k}(t)$ in Equation 3 is defined as

$$\vec{k}(t) = \gamma \int_0^t [g_0(\tau) \ g_x(\tau) \ g_y(\tau) \ g_z(\tau)] d\tau. \quad (4)$$

Powerful diffusion gradients have been shown to alter the actual impulse response $h_{mn}(t)'$ such that $h_{mn}(t)' \neq h_{mn}(t)$.¹⁵ This leads to a change of the apparent k -space trajectory $\vec{k}(t) \rightarrow \vec{k}'(t, \vec{b})$ in Equation 3, where the updated k -space

signal $\vec{k}'(t, \vec{b})$ is given by

$$\vec{k}'(t, \vec{b}) \cong \underbrace{\vec{k}(t)}_{(1) \text{ GIRF-corrected excluding diffusion gradient-induced effects}} + \underbrace{\gamma \cdot \int_0^t \left[\delta g_0(\tau, \vec{b}) \delta g_x(\tau, \vec{b}) \delta g_y(\tau, \vec{b}) \delta g_z(\tau, \vec{b}) \right] d\tau}_{(2) \text{ Diffusion gradient-induced effects}} \quad (5)$$

with δ denoting the deviation with respect to the input gradient waveform. The first term denotes the GIRF-corrected trajectory (excluding the diffusion gradient-induced eddy current correction), and the second term describes the diffusion gradient-induced effects. A schematic representation of these effects is shown in Figure 1, where the GIRF-predicted trajectory including diffusion-encoding gradient waveforms leads to large deviations between the nominal and the actual k -space trajectory, resulting in poor image quality upon reconstruction. In comparison, deviations are reduced and image quality is improved when using the approach according to Equation 5.

Further phase accrual resulting from resonance frequency drifts and concomitant fields introduced by the imaging readout^{25,26} lead to a further extension of Equation 3 to

$$d_c(t, \vec{b}) = \int M_{xy}(\vec{r}, t) \cdot C_c(\vec{r}) \cdot e^{i\vec{k}'(t, \vec{b}) \cdot \vec{r}'} \cdot e^{i\gamma \delta B_0(\vec{r}) t} \cdot e^{i2\pi \delta f_0(t_{scan}) \cdot t} \cdot e^{i\gamma \int_0^t B_C(\vec{r}, \tau) d\tau} \cdot e^{-\vec{b}^T \vec{D}(\vec{r}) \vec{b}} d^3r + \eta, \quad (6)$$

with $\delta f_0(t_{scan})$ the time-dependent global Larmor frequency drift at the time of scanning and $B_C(\vec{r}, t)$ the spatiotemporal readout-induced concomitant field, which can be analytically computed^{29,32} using

$$B_C(x, y, z, t) = \frac{1}{2B_0} \left\{ [G_x^2(t) + G_y^2(t)] z^2 + G_z^2(t) \frac{x^2 + y^2}{4} - G_x^2(t) G_z^2(t) xz - G_y^2(t) G_z^2(t) yz \right\}. \quad (7)$$

An overview of the reconstruction process is shown in Figure 1.

2.2 | Diffusion gradient-induced eddy current measurement

A phase difference approach can be applied to determine the diffusion gradient-induced eddy currents. When disabling the readout gradients, the total phase accrual in the presence of a symmetric set of diffusion gradients can be

described by

$$\varphi(\vec{r}, t) = \gamma \delta B_0(\vec{r}) \cdot t + 2\pi \delta f_0(t_{scan}) \cdot t + \sum_j k_j(t) b_j(\vec{r}) + \varphi_{other}(\vec{r}, t), \quad (8)$$

where the term $\sum_j k_j(t) b_j(\vec{r})$ denotes the linear expansion of the phase accrual of a diffusion gradient for $k_j(t)$ coefficients and $b_j(\vec{r})$ spatial basis functions (see Supporting Information Text S1: GIRF acquisition and processing), and $\varphi_{other}(\vec{r}, t)$ represents an additional phase component unrelated to the diffusion gradient. Because the diffusion gradients are symmetric with respect to the echo pulse, the effective concomitant field at the point of readout is canceled out and can therefore be ignored.³³ Measuring a volume once with standard and once with inverted diffusion gradient polarity enables the extraction of the linear expansion term. By taking the phase difference after correcting for Larmor frequency drifts per imaged voxel, the linear responses are summed, whereas terms for off-resonances and phases not related to the diffusion gradients are canceled out.³⁴

2.3 | Image reconstruction

Because the encoding process is bandwidth (BW)-limited, describing Equation 6 in a discretized matrix-vector form using a similar formalism as given in^{24,35} yields

$$\vec{d} = E \vec{\rho} + \vec{\eta}, \quad (9)$$

where $\vec{\rho}$ is a vector representation of the rasterized object and \vec{d} the encoded k -space signal given encoding matrix E and Gaussian noise $\vec{\eta}$. We now introduce the notation $E = \vec{E} \circ \vec{E}$ for element-wise multiplication and define

$$\vec{E}_{(c, \kappa), \lambda} = e^{i\vec{k}'(t_{\kappa}, \vec{b}) \cdot \vec{r}'_{\lambda}}, \quad \vec{E}_{(c, \kappa), \lambda} = e^{\underbrace{i\gamma \delta B_0(\vec{r}_{\lambda}) t_{\kappa}}_{(1)} + \underbrace{i\gamma \int_0^{t_{\kappa}} B_C(\vec{r}_{\lambda}, \tau) d\tau}_{(2)} + \underbrace{i\vec{k}'_z(t_{\kappa}, \vec{b}) r_{z, \lambda}}_{(3)}},$$

which encompasses regular Fourier-encoding ($\vec{E}_{(c, \kappa), \lambda}$) and additional encoding terms ($\vec{E}_{(c, \kappa), \lambda}$) with sampling time points κ and number of grid points λ . $\vec{E}_{(c, \kappa), \lambda}$ represents the superposition of encoding phases arising from (1) off-resonances and (2) trajectory-induced concomitant fields. When solely using 2D gridding, term (3) is used to correct for the through-slice component but can be omitted when using a 3D gridding approach because the effect is absorbed by the 3D trajectory.

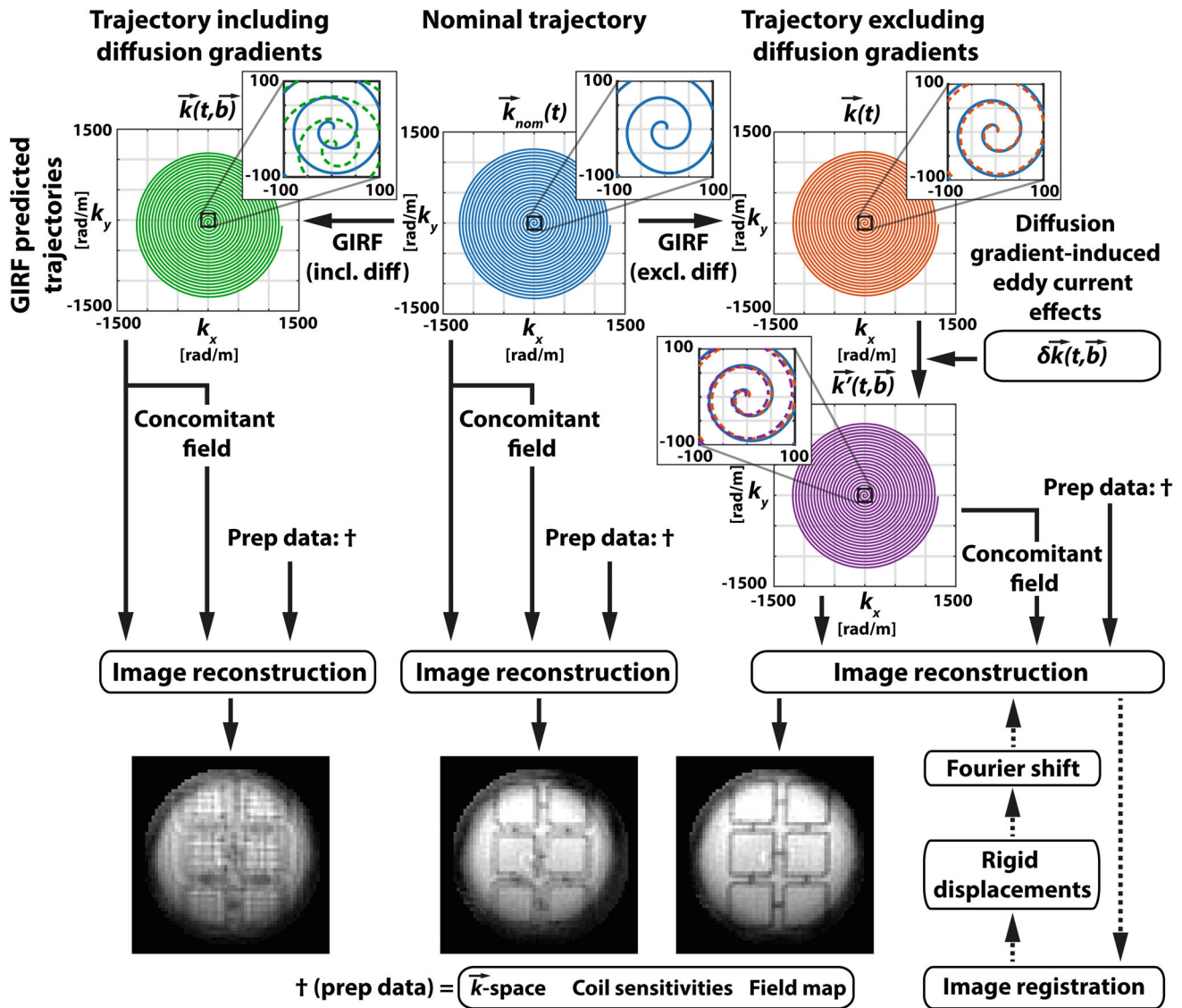


FIGURE 1 Schematic overview of the trajectory prediction and image reconstruction process using a spiral trajectory example. When taking the nominal trajectory $\vec{k}_{nom}(t)$ (blue), the reconstruction process converts the raw \vec{k} -space data using the off-resonance field map, coil sensitivities, and trajectory-induced concomitant fields into an image with a residual level of blurriness. When including the diffusion gradients (incl. diff) and predicting the trajectory with a GIRF, a distorted trajectory $\vec{k}(t, \vec{b})$ (green) with respect to the nominal trajectory is obtained. When excluding the diffusion gradients (excl. diff) in the GIRF prediction, we obtain trajectory $\vec{k}(t)$ (orange), which differs from the nominal trajectory. Updating the trajectory including diffusion gradient-induced eddy current effects, $\delta\vec{k}(t, \vec{b})$, leads to trajectory $\vec{k}'(t, \vec{b})$. The in vivo protocol additionally registers the initial data from the GIRF (excl. diff) path, extracts the rigid displacements, and performs alignment of the \vec{k} -space data using the Fourier shift theorem (dashed arrows). GIRF, gradient impulse response function.

Whereas $\bar{E}_{(c,\kappa),\lambda}$ can efficiently be evaluated using iterative reconstruction, $\tilde{E}_{(c,\kappa),\lambda}$ can be time-consuming to compute depending on κ and λ . A common approach is to apply singular value decomposition (SVD) $\tilde{E} = U\Sigma V$ followed by singular-value thresholding to approximate $\tilde{E} = \tilde{E}_L$ by L separable functions^{18,35}

$$\tilde{E}_L = \sum_{l=1}^L c_l b_l^H, \quad (10)$$

with $[c_1, c_2, \dots, c_L] := U$ and $[b_1, b_2, \dots, b_L] := V\Sigma^H$. To reduce computation time, we propose the use of a random SVD algorithm to efficiently find the (lowest) optimal number of singular-value components (L).³⁶

3 | METHODS

All imaging was performed on a clinical 1.5 Tesla Philips Achieva System (Philips Healthcare, Best, The

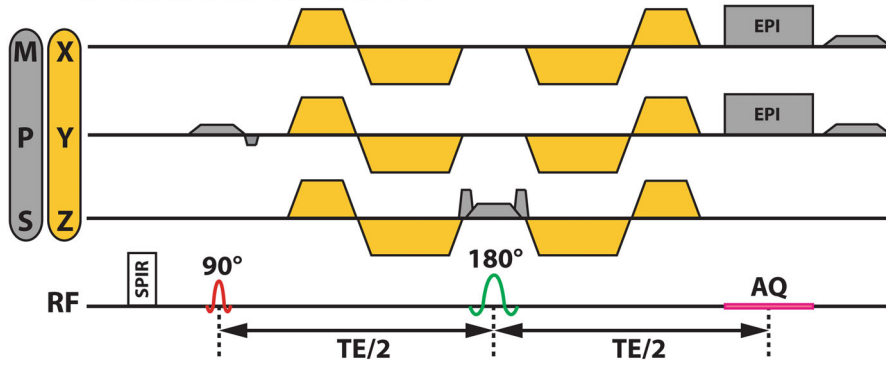
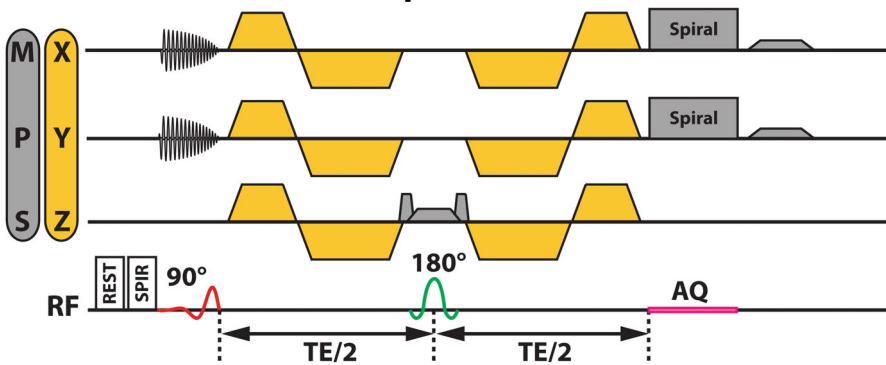
(A) 2nd order MC-SE 2D ssh-EPI(B) 2nd order MC-SE 2D ssh-Spiral

FIGURE 2 Schematic overview of the EPI and spiral cDTI sequences. (A) Second-order MC-SE ssh 2D EPI sequence, and (B) second-order MC-SE ssh 2D spiral sequence. The diffusion gradients are oriented along the gradient system axis (XYZ; yellow), while other gradients are positioned according to the measurement orientation (MPS; gray). The 90° excitation pulse is in red, and the echo pulse is in green. AQ marks data acquisition (pink). cDTI, cardiac DTI; MC-SE, motion-compensated spin-echo; ssh, single shot; REST, regional saturation; SPIR, spectral presaturation with inversion recovery.

Netherlands) with maximum gradient strength of 80 mT/m at a slew rate of 100 T/m/s.

3.1 | General features

The following generic sequence design elements were implemented. Crusher gradients placed around the echo pulse were solely active when acquiring the $b = 0$ s/mm² data because the second-order MC waveforms crush spurious signals. Spoiler gradients were placed at the end of the sequence readout. All sequences were programmed to have identical slice-selective echo-pulse gradient amplitude and slope durations, slew rate, echo-pulse B_1 strength, and diffusion gradient timings.

Fat suppression was performed using spectral presaturation with inversion recovery,^{37,38} and a respiratory navigator was placed on the right hemidiaphragm with a 5 mm acceptance window to ensure consistent breath-holding. Dynamic δf_0 fluctuations were corrected for using the method described in the Supporting Information Text S2: Dynamic δf_0 stabilization.

3.2 | EPI sequence

The EPI cDTI sequence is schematically depicted in Figure 2A. The respiratory navigator precedes the

sequence, followed by the δf_0 update (not shown). The spectral presaturation with inversion recovery pulse is applied prior to non-coplanar excitation (90° selective along phase-encoding direction) to achieve a reduced FOV.³⁹ The second-order MC diffusion gradients are placed symmetrically around the echo pulse.^{12,13,40}

Acquisition parameters were: FOV = 220 × 110 × 8 mm³, in-plane acquired/zero-filled resolution = 2.5 × 2.5 mm²/1.25 × 1.25 mm², signal averages = 11, TR = 1 s, TE = 92 ms, flip angle $\alpha = 90^\circ$, and BW_{epi}/pixel = 31.4 Hz/pixel (at 2.5 × 2.5 mm² in-plane resolution)/echo-spacing = 0.7 ms.

3.3 | Spiral sequence

The spiral cDTI sequence is shown in Figure 2B. The respiratory navigator precedes the sequence, followed by the δf_0 update (not shown). Regional saturation slabs placed circularly around the field of excitation saturate the signal, followed by spectral presaturation with inversion recovery fat suppression and 2D RF excitation normal to the slice to achieve a reduced field of excitation.^{41,42} Simulations of the 2D RF pulse can be found in Supporting Information Figure S2 and Supporting Information Text S3: 2D RF excitation beam simulation.

Acquisition parameters were: FOV = 150 × 150 × 8 mm³ (including 25% in-plane

oversampling), in-plane acquired/zero-filled resolution = $2.5 \times 2.5 \text{ mm}^2 / 1.25 \times 1.25 \text{ mm}^2$, signal averages = 11, TR = 1 s, TE = 57 ms, $\alpha = 90^\circ$, spiral readout duration = 26 ms, spiral sampling rate = $5.4 \mu\text{s}$, and 10 rectangular regional saturation slabs of 80 mm width placed in circular orientation around the field of excitation. 2D RF parameters were: beam diameter = 110 mm, $k_{max} = 170 \text{ rad/m}$, 16 turns, and duration of 7.23 ms.

3.4 | B_0 measurement

A double gradient-echo sequence was used to acquire a field map with the following acquisition parameters: FOV = $210 \times 210 \times 8 \text{ mm}^3$, in-plane resolution = $1 \times 1 \text{ mm}^2$, TR/TE/ ΔTE = 11.1/4.5/4.5 ms, $\alpha = 20^\circ$, trigger delay (TD) $\text{TD}_{B_0} = \text{TD}_{\text{DTI}} + \text{TE}_{\text{DTI}}$ (to ensure temporal alignment of the field map with the TE of the cDTI scan), and a total field map acquisition duration of 21 s.

3.5 | Diffusion measurements

All in vivo data measurements were triggered using a vectorcardiogram with a TD (time between detection of R-wave and application of first RF pulse) set to 65% peak systole. In total, 9 diffusion directions (Supporting Information Table S1, and briefly discussed in Supporting Information Text S4) were characterized at b values 150 s/mm^2 and 450 s/mm^2 . For in vivo imaging, similar to,⁸ 3 orthogonal directions of b value 150 s/mm^2 and 9 directions with 450 s/mm^2 were used (Supporting Information Table S2). The diffusion gradient directions were fixed to the gradient system axes (see Figure 2).

3.6 | GIRF measurement sequence

A sequence to measure the GIRF was implemented according to the work of Rahmer et al.³⁰ In short, multiple thin off-center slices were excited and spatially encoded using in-plane phase-encoding. A through-slice chirp test gradient was applied with regular and inverted sign to obtain phase difference measurements. Additional information can be found in Supporting Information Text S1: GIRF acquisition and processing.

3.7 | Diffusion gradient-induced eddy current measurement sequence

To measure eddy currents originating from the diffusion gradients (which are not captured by the GIRF), the sequence shown in Figure 2B was modified to include

3D phase-encoding gradients placed directly in between 2D RF excitation and the first diffusion gradient lobe (Figure 3A). The slice-selective gradient at the echo-pulse was disabled, and data acquisition was performed with a user-specified BW and acquisition window. The diffusion gradient waveforms were inverted to allow phase difference measurements. The main difference to the work of Rahmer et al.³⁰ is that no gradients were played out during the readout, allowing the measurement of a full 3D volume with isotropic voxel size.

A spherical phantom (16-cm diameter) filled with silicone oil (AK 500, Wacker Chemie AG, Munich, Germany) was placed inside the scanner at the isocenter and imaged using a 5-channel cardiac coil. Thanks to the very low diffusivity of silicone oil, it permits a minimal SNR penalty when applying diffusion gradients and exhibits a sufficiently high T_2^* value.⁴³ 3D scan parameters were FOV = $210 \times 210 \times 210 \text{ mm}^3$, matrix size = $7 \times 7 \times 7$ voxels, signal averages = 1, TR = 1 s, acquisition window = 150 ms, acquisition bandwidth = 32 kHz, 2D RF excitation beam diameter = 250 mm, 19 diffusion directions ($1 \times b = 0 \text{ s/mm}^2$ (used as δf_0 navigator), $9 \times b = 150 \text{ s/mm}^2$, and $9 \times b = 450 \text{ s/mm}^2$), and a total acquisition time of 217 min. A schematic overview of the 3D voxel grid with respect to the silicon oil sphere is shown in Figure 3B. A single eddy current characterization measurement was performed to correct both EPI and spiral cDTI sequences at arbitrary slice angulations and offsets. An overview of the data processing is given in Supporting Information Figure S3 and in Supporting Information Text S5: Diffusion gradient-induced eddy current data processing.

3.8 | Phantom

A silicone ice cube tray (2×3 grid, Migros, Zurich, Switzerland) was placed in a cylindrical container and filled with 2% agarose gel (Sigma-Aldrich, St. Louis, MO) with 0.75 g/L copper-sulfate (Honeywell Fluka, Seelze, Germany). Using a 5-channel cardiac coil array, a single coronal slice was imaged with offsets of $+4.9/-7.4/+36.5 \text{ mm}$ along the X, Y, and Z directions of the scanner's gradient system axes, respectively, with the phantom placed at a 30-degree angle along the $-Y$ and $+Z$ plane. Data was acquired with 2 signal averages using the sequences presented in Figure 2A,B, excluding the spectral presaturation with inversion recovery pulses. Dynamic δf_0 correction was not enabled given the short scan duration (40 s).

3.9 | Ex vivo

A porcine heart was obtained⁴⁴ and prepared as described in Supporting Information Text S6: Ex vivo heart

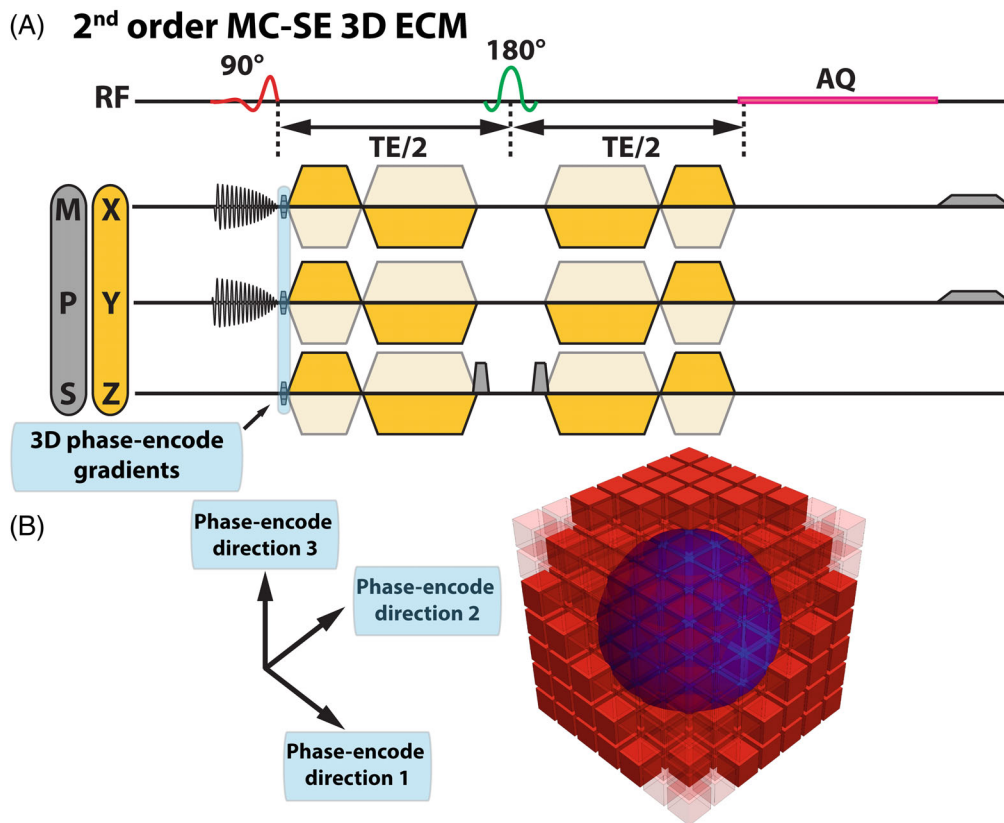


FIGURE 3 Schematic overview of the diffusion gradient-induced ECM sequence. (A) Second-order MC-SE 3D diffusion gradient-induced ECM sequence. With the ECM sequence, a $7 \times 7 \times 7$ grid was measured with standard and inverted diffusion gradient polarity. Phase-difference data is fitted to third-order spherical harmonics to obtain zeroth- and first-order diffusion gradient-induced eddy current contributions for each diffusion direction. The light-blue area in (A) highlights the position of the 3D phase encode gradients. Light-yellow colored gradients indicate inverted diffusion gradients. The diffusion gradients are oriented along the gradient system axis (XYZ; yellow), whereas other gradients are positioned according to the measurement orientation (MPS; gray). The 90° excitation pulse is in red, and the echo-pulse is in green. AQ marks data acquisition (pink). (B) Schematic overview of 3D encoding of the diffusion gradient-induced eddy currents. A silicon oil sphere (16 cm in diameter) is imaged using a $7 \times 7 \times 7$ 3D voxel grid with a FOV of $21 \times 21 \times 21$ cm^3 . MC-SE, motion-compensated spin-echo; ECM, eddy current measurement.

preparation and imaged using a 5-channel cardiac coil and a single short-axis mid-ventricular slice using 2 signal averages at respective offsets of $-47.9/-4.2/-4.8$ mm along the X, Y, and Z directions of the scanner's gradient system axes. Dynamic δf_0 correction was not enabled given the short scan duration (40 s).

3.10 | In vivo

Eight volunteers (5 male, 3 female, age 25 ± 4 years, heart rate 61 ± 7 bpm) were imaged using a 32-channel cardiac array coil upon written informed consent according to ethical and institutional requirements. A single-slice in short-axis orientation was acquired at midventricular level, with both EPI and spiral sequences as described in the sequence design section.

All in vivo cDTI acquisitions were performed during repetitive breath-holding corrected for heart

rate-dependent relaxation differences as described in Supporting Information Text S7: Heart rate correction. The δf_0 stabilization measurement was performed at the start of each breath-hold. Due to breath-hold inconsistencies, 1 data set was excluded from further analysis. The first average of each acquisition series was excluded from further processing. Field maps for each in vivo cDTI sequence type were acquired in a separate breath-hold scan with a FOV of $322 \times 279 \times 8$ mm^3 , an acquisition window per heart-beat = 267 ms, and a total scan duration of approximately 24 s.

3.11 | Data reconstruction

Field map reconstruction was performed offline using MRecon (version 4.2.0, GyroTools LLC, Winterthur, Switzerland). Otsu's method⁴⁵ was applied to the first TE magnitude image to generate a global mask. Median

filtering, denoising, and extrapolation of the field map^{46,47} were applied prior to reslicing the field map to the cDTI geometry. An example field map is shown in Supporting Information Figure S4.

Coil sensitivities and cDTI data were prepared including array coil compression of the 32-channel coil data to 10 virtual coils.⁴⁸ The GIRF-predicted trajectory was updated for each diffusion direction using first-order eddy current coefficients according to Equation 5 and subsequently used to compute the trajectory-induced concomitant fields as described by Equation 7. Zeroth-order diffusion gradient-induced eddy currents were corrected for by demodulating the k -space signal prior to image reconstruction. All data was reconstructed at $2.5 \times 2.5 \text{ mm}^2$ and zero-filled to $1.25 \times 1.25 \text{ mm}^2$ in-plane resolution. Gradient channel delays were identified for each EPI dataset to identify the point of minimum Nyquist ghosting, and the same setting was applied for the corresponding spiral data.

Using a conjugate-gradient algorithm penalizing first-order differences, Equation 9 was inverted^{18,49} using 2D nonuniform fast Fourier transforms during forward and backward operations and SVD decomposition of $\tilde{E}_{(c,\kappa),\lambda}$. In the spiral case, a circular mask with a diameter of 90% of the FOV was used to suppress regions outside the field of excitation during reconstruction. Raw k -space data and coil sensitivities were prewhitened to remove noise correlations.⁴⁹ Number of iterations: 10 (phantom, ex vivo) and 2 (in vivo).

To evaluate the proposed reconstruction approach, we define the *reference reconstruction* approach to include GIRF trajectory prediction (excluding GIRF cross-terms), off-resonance, and concomitant field corrections. A second reconstruction, additionally correcting for the zeroth- and first-order diffusion gradient-induced eddy currents, is referred to as the *proposed reconstruction*. For the in vivo data, the *proposed reconstruction* approach data was registered, and rigid in-plane displacements⁵⁰ were extracted and then used to align the data to the field map prior to the final proposed reconstruction to account for breath-hold inconsistencies. All reconstruction tasks were performed using MatLab (version 9.9.0, MathWorks, Natick, MA).

3.12 | Data analysis

3.12.1 | Eddy current analysis

To assess nonlinearity of the diffusion gradient-induced eddy currents and express the signal in SNR units, a corresponding noise signal was generated as described in Supporting Information Text S8: Eddy current analysis noise signal. Eddy current nonlinearity was then examined using the zeroth- and first-order eddy current responses as

follows. Per eddy current coefficient and per b value, an SVD was performed on the matrix containing the temporal responses of all 9 diffusion directions according to $N_{dirs} \times t$, where only the first 40 ms of the signal were selected for the SVD. The simulated noise of each eddy current response was projected onto the same basis and the temporal SD of the signal was determined. SNR units were obtained by dividing the values of each eddy current response by the respective noise SD.

3.12.2 | Phantom/ex vivo

Upon image reconstruction, tensors were calculated using the data from b values 150 s/mm^2 and 450 s/mm^2 ,⁵¹ and mean diffusivity (MD) and fractional anisotropy (FA) were examined for each reconstruction case using a region of interest and then reported using mean and SD.

Ex vivo data was processed similarly to the phantom data. In addition, the helix angle (HA), transmural helix angle gradient, transverse angle (TA), and absolute sheetlet angle (E2A) were determined.^{52,53} Registration was not performed on the phantom and ex vivo data to highlight differences between the reference and proposed reconstruction approach.

3.12.3 | In vivo

After data reconstruction, nonrigid registration⁵⁰ was applied prior to tensor calculation, followed by determination of MD, FA, HA, helix angle gradient, TA, and E2A. A left-ventricular (LV) region of interest was used to determine mean and SD values of all cDTI metrics. Normalized absolute difference (NAD) was computed per diffusion direction according to $NAD(\epsilon_{\vec{b}}) = \text{abs}(\epsilon_{prop,\vec{b}} - \epsilon_{ref,\vec{b}}) / \left\| \text{abs}(\epsilon_{ref,\vec{b}}) \right\|$, with $\epsilon_{\vec{b}}$ the diffusion weighted image of the proposed ($\epsilon_{prop,\vec{b}}$) or reference ($\epsilon_{ref,\vec{b}}$) reconstruction.

4 | RESULTS

4.1 | Eddy current analysis

In Figure 4, zeroth- and first-order eddy current responses are plotted for the orthogonal diffusion directions aligned with the gradient system axes for b values 150 s/mm^2 and 450 s/mm^2 . Tripling the b value does not lead to corresponding scaling of the eddy current responses in all cases, for example, as the zeroth-order response for the +X gradient exhibits a different profile for 150 s/mm^2 compared

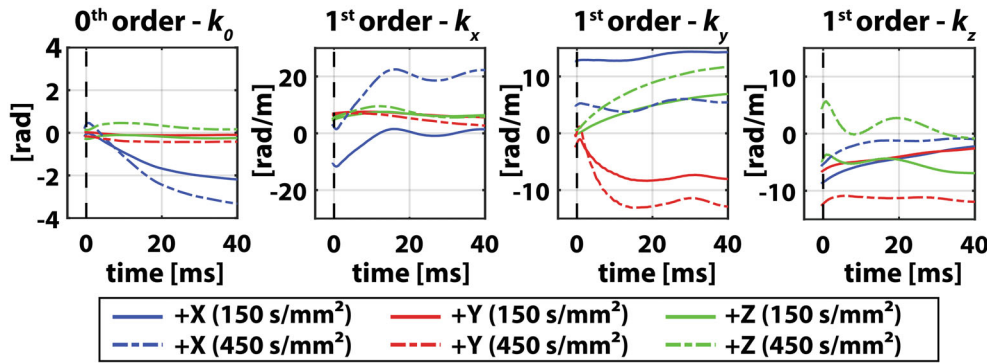


FIGURE 4 Overview of zeroth- and first-order diffusion gradient-induced phase evolutions for 3 orthogonal diffusion directions recorded for b values of 150 s/mm^2 and 450 s/mm^2 . The dashed black line represents the TE.

to 450 s/mm^2 . Data for other diffusion directions can be found in Supporting Information Figure S5.

Supporting Information Figure S6 shows the SVD components of the zeroth- and first-order diffusion gradient-induced eddy currents for b values 150 s/mm^2 and 450 s/mm^2 in SNR units. For $b = 150 \text{ s/mm}^2$, the singular values decrease below the noise floor ($\text{SNR} = 1$) at SVD component 5. For $b = 450 \text{ s/mm}^2$, the SVD components for the z -eddy current do not drop below the noise floor until SVD component 7 is reached.

4.2 | Phantom

The effects of sequentially adding compensations for trajectory and/or magnetic field imperfections during reconstruction for a single diffusion direction are visualized in Figure 5. MD and FA maps of the structure phantom are shown in Figure 6. For the reference reconstruction, the MD maps for both EPI and spiral cDTI data display lower values due to blurring in areas where a physical border exists. In case of spirals, this effect is equally distributed across the FOV, whereas for EPI it is predominantly present along the phase-encoding direction. Using the proposed reconstruction approach, MD and FA maps appear more homogeneous for both spiral and EPI readouts.

MD values in the region of interest change from 2.01 ± 0.16 to $2.02 \pm 0.04 \times 10^{-3} \text{ mm}^2/\text{s}$ for the spiral case and from 2.04 ± 0.09 to $2.05 \pm 0.05 \times 10^{-3} \text{ mm}^2/\text{s}$ in the case of EPI using the proposed reconstruction. FA values respectively decrease from 0.15 ± 0.11 to 0.05 ± 0.03 and from 0.12 ± 0.10 to 0.06 ± 0.03 for the spiral and EPI cases.

4.3 | Ex vivo

An overview of the ex vivo cDTI metric maps are shown in Figure 7. The proposed reconstruction approach offers improvements of HA maps for both EPI and spiral data. For EPI, the endo-/epicardial borders exhibit less noisy

appearance, and smoother HA transitions over the transmural extent are observed. For spiral cDTI, the proposed reconstruction reduces artifacts in the entire LV HA map. After diffusion gradient-induced eddy current correction, hyperintense regions in the TA, E2A, and FA maps are reduced for EPI data. MD maps remain comparable between both reconstruction cases.

In the spiral case, the proposed reconstruction eliminates hyperintense areas in the heart wall in the TA map and yields an E2A map similar to EPI. Compared to the reference reconstruction, the MD map is in better agreement with the EPI case. Most noticeably in the FA map, hyperintense signal areas are reduced after correction of diffusion gradient-induced eddy currents. Corresponding data can be found in Supporting Information Figure S7, which demonstrates that distributions of EPI and spiral cDTI data are in closer agreement with the proposed reconstruction.

4.4 | In vivo

An overview of the in vivo EPI and spiral k -trajectories is given in Figure 8, including relative differences between the proposed and reference reconstruction. The maximum k_0 phase excursion for both trajectories is between -1.7 rad for EPI and -1.5 rad for spiral. For the first-order terms (k_x, k_y, k_z), the maximum trajectory differences are between -10 rad/m and -14 rad/m for EPI and between -16 rad/m to $+12 \text{ rad/m}$ for spiral. Neither trajectory reaches the nominal resolution of $\pm 1250 \text{ rad/m}$, corresponding to a $2.5 \times 2.5 \text{ mm}^2$ in-plane resolution.

An overview of the reconstructed in vivo magnitude data for all diffusion directions is shown in Supporting Information Figure S8. The proposed reconstruction mainly results in changes along the phase encode direction for EPI and conserves general image shape. Conversely, the spiral images exhibit noticeable differences between the reconstruction cases, which are emphasized in the LV and liver. The LV is sharper after the proposed reconstruction, with large changes around the anterolateral heart

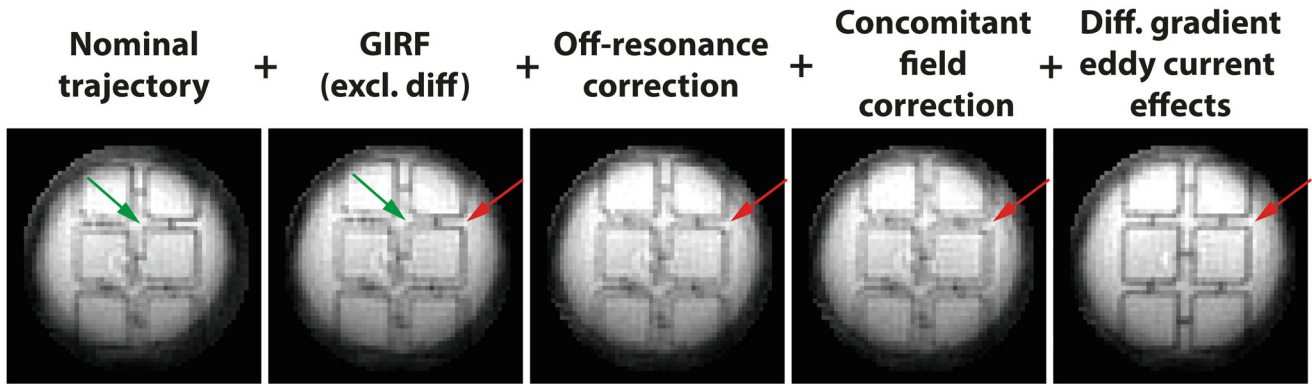
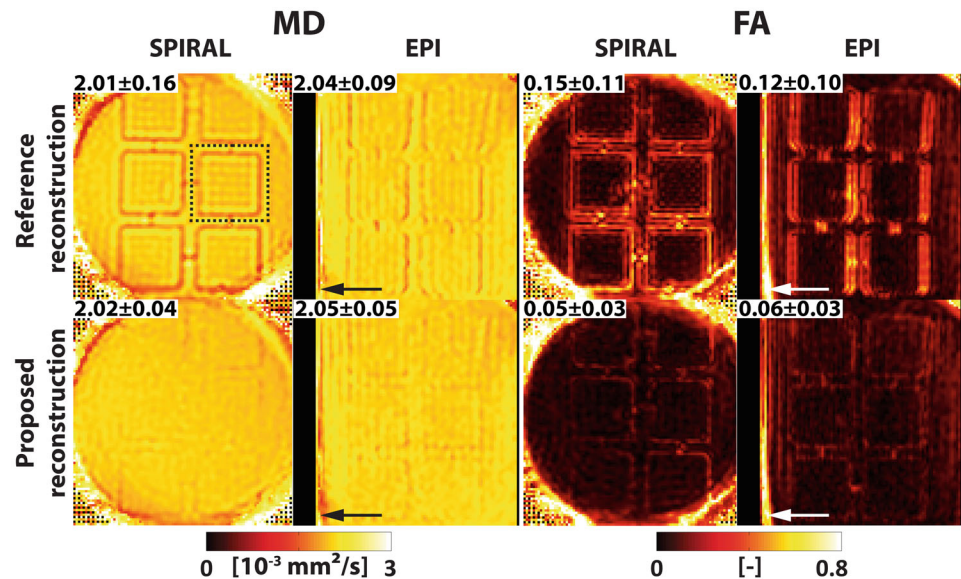


FIGURE 5 Example of sequential compensation of trajectory and/or magnetic field imperfections for a single diffusion direction acquired with a spiral readout. Starting with the nominal k -space trajectory, the effect of sequentially adding the GIRF-prediction (excluding diffusion gradients), off-resonance correction, trajectory-induced concomitant field correction, and correction of diffusion gradient-induced eddy current effects is shown

FIGURE 6 MD and FA maps of the structure phantom acquired with spiral and EPI readouts. The top row displays the maps obtained using the reference reconstruction approach. The bottom row shows the maps using the proposed reconstruction approach. The ROI is indicated with the dashed black line. The phase encoding direction of the EPI data is shown with black (in MD maps) and white (in FA maps) arrows. Inset values indicate ROI values expressed in mean \pm SD FA, fractional anisotropy; MD, mean diffusivity; ROI, region of interest.



wall perimeter and the inferior LV liver interface (Supporting Information Figure S8, white arrow).

Example in vivo reconstruction cases are displayed in Figure 9. EPI data shows minimal differences between the reconstruction approaches. In the spiral case, the mean DWI of the proposed reconstruction approach results in sharper image appearance. HA maps display smoother transmural changes in the epicardial/endocardial border regions with fewer outliers. Distorted areas in the HA and TA maps can be observed in the inferolateral wall. Reduced TA regions can be noted in the inferolateral wall, and more elevated regions are found in the E2A map. MD appears reduced at the epicardial/endocardial border regions. Most noticeable in the FA map is a regional reduction of FA in the inferior heart wall section. Corresponding distributions plotted in Supporting Information Figure S9 confirm

minimal apparent changes for EPI but noticeable changes in HA, E2A, MD, and FA metrics for spiral.

Figure 10 displays an overview of all in vivo cDTI metrics for both EPI and spiral data. For EPI, the differences between the reconstructions are subtle, whereas for spiral the proposed methods lead to a reduction in mean and SD of MD and FA. Overall, higher MD and lower FA are observed for spirals with a trend toward lower SDs compared to EPI. For EPI, the helix angle gradient, E2A, and TA mean values are similar overall, whereas a noticeable spread can be observed for spiral. The corresponding SDs exhibit comparable ranges between methods.

The in vivo SNR analysis in Supporting Information Figure S10 shows a 1.8-fold increase in mean SNR and 2.5-fold increase in SD for spirals across all diffusion directions compared to EPI.

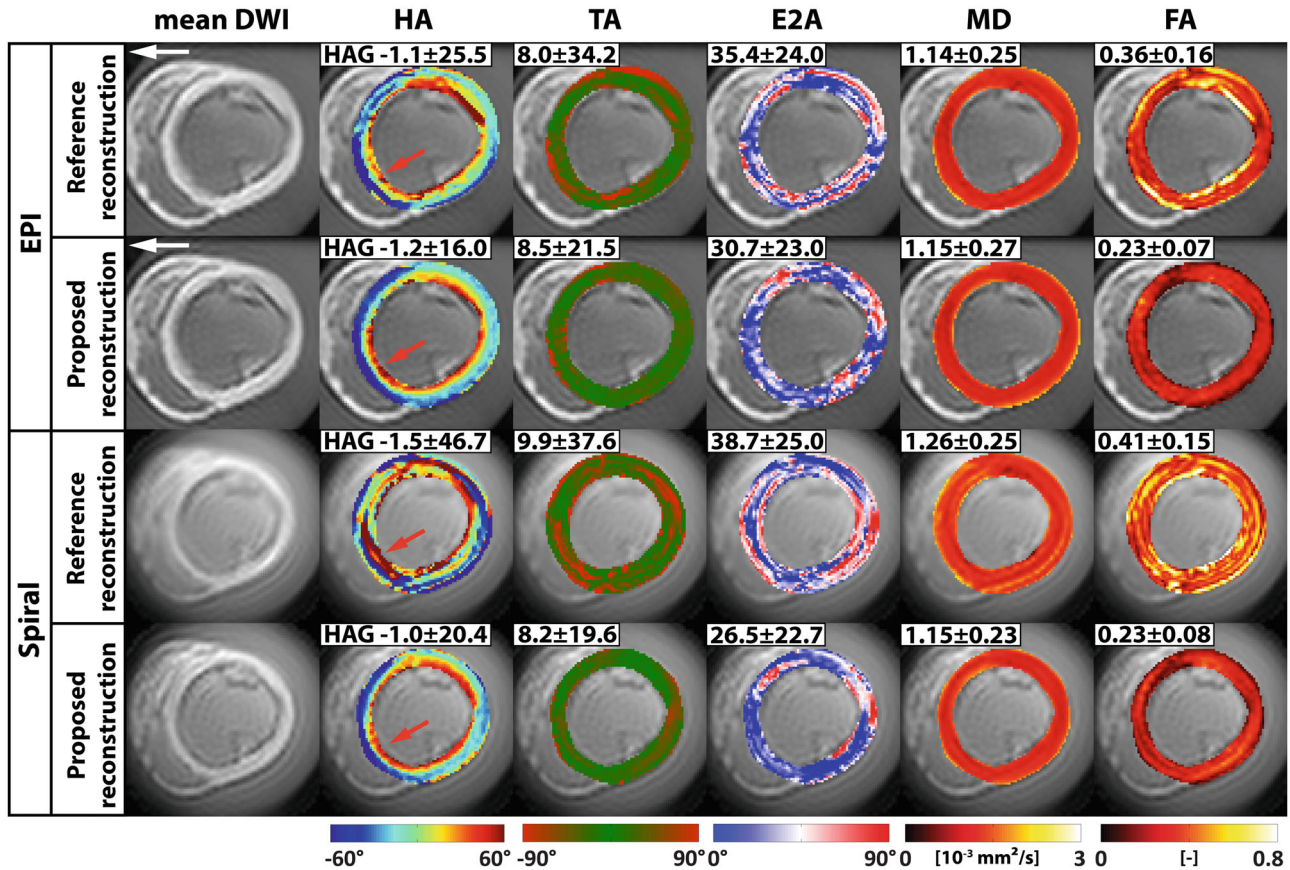


FIGURE 7 Ex vivo porcine heart acquired with EPI and spiral cDTI protocols. For EPI and spiral trajectories, the reference and proposed reconstructions are shown with their respective mean DWI, HA, TA, E2A, MD, and FA maps. Inset values display the mean \pm SD values in the LV. For the HA maps, the HAG values in $^\circ/\%$ -transmural depth are shown. The white arrows indicate the phase encoding direction for EPI. The red arrow indicates the endocardial septal wall area. E2A, absolute sheetlet angle; HA, helix angle; HAG, helix angle gradient; TA, transverse angle; MD, mean diffusivity; FA, fractional anisotropy.

5 | DISCUSSION

In this work, eddy currents induced by second-order MC diffusion gradients have been characterized, demonstrating nonlinear behavior and hence the need for dedicated correction steps in echo-planar and spiral cDTI data processing. Our proposed correction approach provided good image congruency in phantom and ex vivo data, addressing artifacts in MD, FA, and other cDTI maps. The ability of the method to correct diffusion gradient-induced eddy current image distortions in vivo was demonstrated, highlighting particular benefits for second-order MC-SE spiral cDTI.

To our knowledge, only Gorodezky et al. have explored the use of spirals for in vivo cDTI.^{16,17} They demonstrated the benefits of an in vivo multi-shot spiral cDTI STEAM sequence to achieve higher spatial resolution compared to a twofold undersampled EPI readout. Because DW-STEAM sequences do not require strong gradient systems, diffusion gradient-induced eddy currents were assumed to be negligible.⁵⁴ Their approach of

measuring field maps using a low-resolution spiral for each acquisition could capture both static f_0 and δf_0 variations in a convenient manner. The lower resolution of the field map, however, would not allow to correct for issues at tissue interfaces.⁴⁷ Conversely, our approach of capturing δf_0 variations using the dynamic stabilization option requires the volume to be consistent per breath-hold. Using free-breathing, such an approach could fail because the excited volumes may differ. Compared to our work, Gorodezky et al. did not use a GIRF to predict the trajectory.

The in vivo results suggest that the use of a spiral readout leads to higher MD and lower FA values, which is in agreement with Gorodezky et al., who compared multi-shot spiral with single-shot EPI STEAM-cDTI.¹⁶ Because the SNR is lower with EPI than for spiral, the enhanced noise levels could lead to an increased underestimation of the MD and overestimation of FA due to eigenvalue repulsion.^{55,56} Because off-resonance artifacts affected the inferolateral heart wall, a statistical data analysis would lead to biases, as can be seen in Figure 10

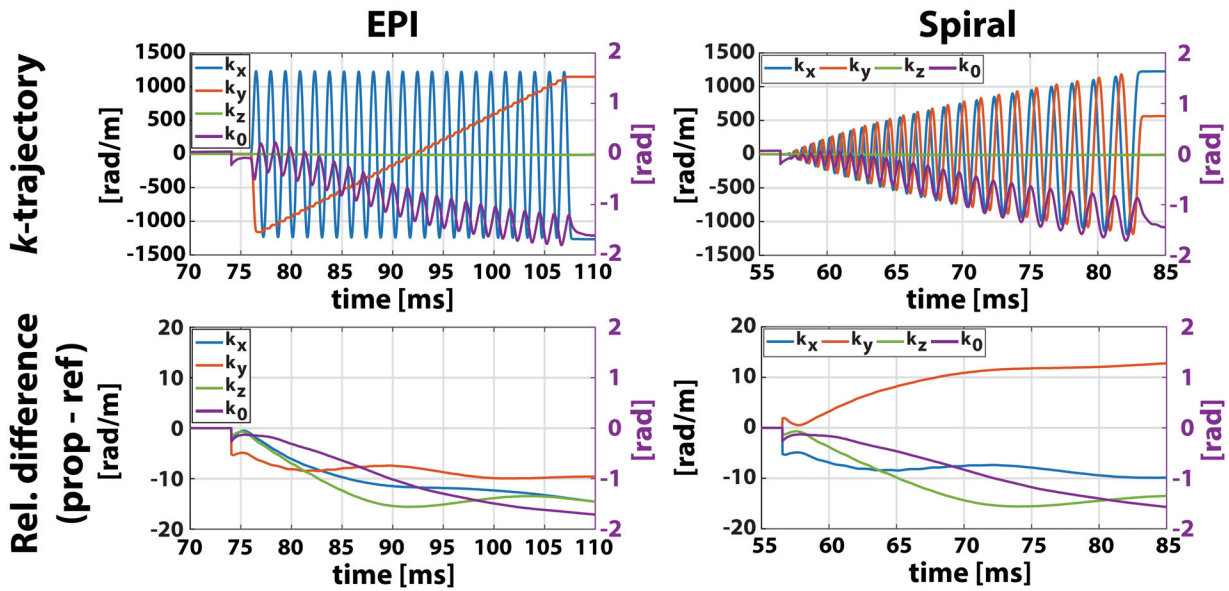


FIGURE 8 Example k -space trajectories of the proposed reconstruction for EPI and spiral (top row) and their relative differences with respect to the reference reconstruction (bottom row). Trajectories are taken from in vivo cDTI data for diffusion direction 8 (Supporting Information Figure S8). Note the presence of a dedicated y -axis for the k_0 component with a different scale and unit. prop, proposed; ref, reference; rel., relative.

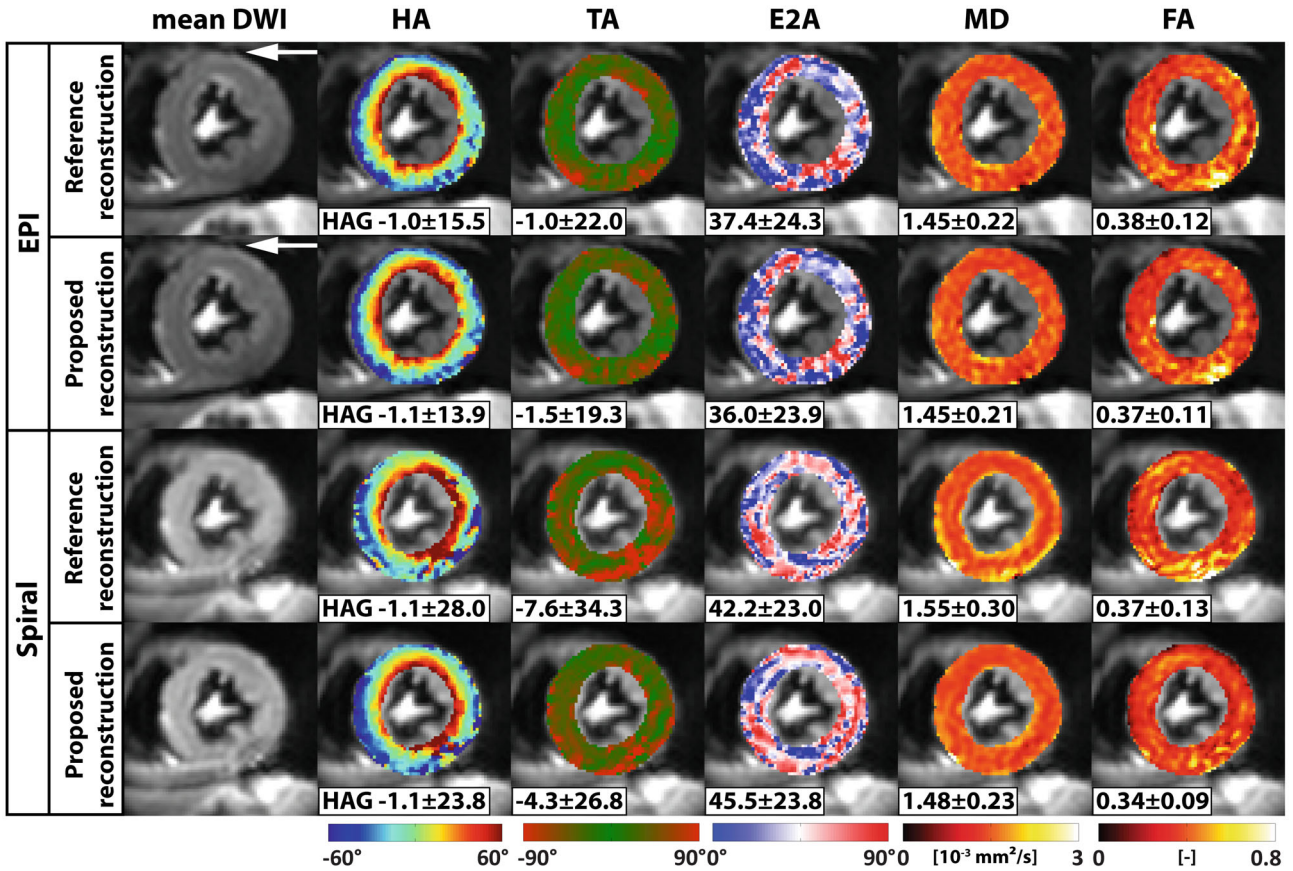


FIGURE 9 Example in vivo cDTI data acquired using spiral and EPI readouts and reconstructed using the reference and proposed approach. EPI (top rows) and spiral (bottom rows) are shown with their respective reconstruction cases and display mean DWI, HA, TA, E2A, MD, and FA maps. Inset values display the mean \pm SD values in the LV. For the HA maps, the transmural HAG values in $^\circ/\%$ -transmural depth are shown. The white arrows indicate the phase encode direction for EPI. E2A, absolute sheetlet angle; HA, helix angle; HAG, helix angle gradient; TA, transverse angle; MD, mean diffusivity; FA, fractional anisotropy; LV, left-ventricular.

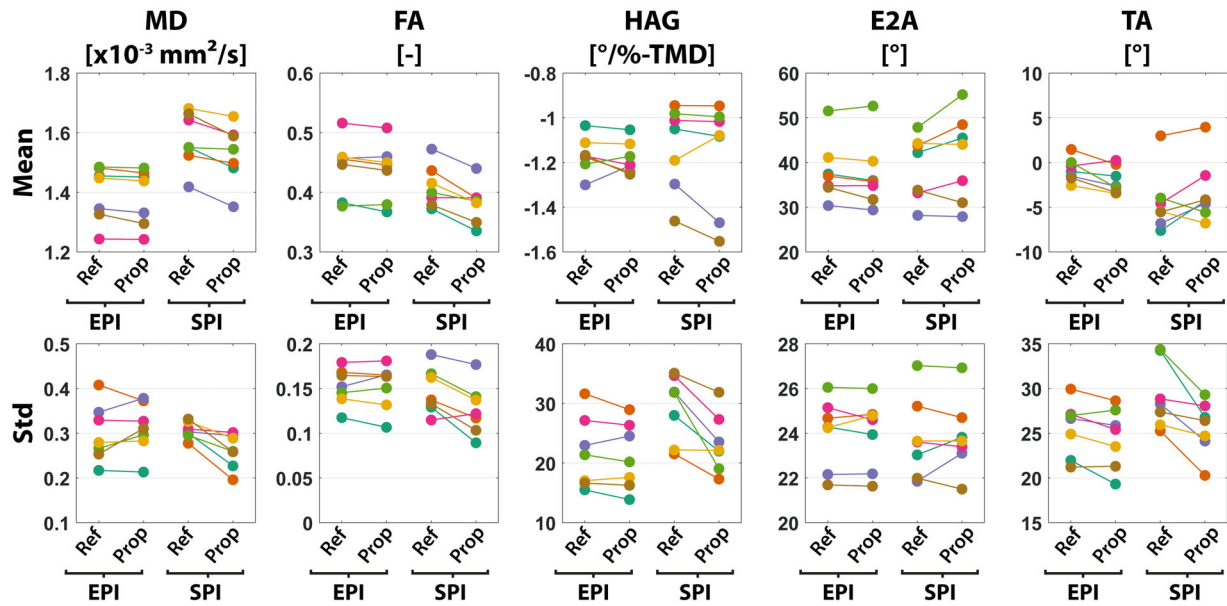


FIGURE 10 In vivo cDTI metric overview of all volunteers. LV mean and SD are plotted for each volunteer for the ref and prop approaches for EPI and SPI. SPI, spiral imaging; MD, mean diffusivity; FA, fractional anisotropy; HAG, helix angle gradient; E2A, absolute sheetlet angle; TA, transverse angle; ref, reference; prop, proposed.

given the wider spread of helix angle gradient and TA metrics. Further research is required to alleviate off-resonance artifacts to permit a complete statistical analysis.

The presented approach performed image reconstruction at the acquisition resolution. The use of high-resolution field maps could further improve image quality in critical areas such as the inferolateral heart wall, where strong field gradients are often present.⁴⁷ Iterative reconstruction using 10 iterations offered adequate reconstruction of phantom and ex vivo cDTI data. In vivo spiral cDTI data experienced diverging reconstruction behavior for varying diffusion directions, and a maximum of 2 iterations was applied. We hypothesize that variations in LV SNR and magnetic field gradient strength at the posterior vein are contributing factors, which should be examined in more detail.

Our work was limited by the accuracy of the eddy current characterization approach. Higher-order eddy currents could have further contributed to image artifacts but remain challenging to characterize due to the limited SNR of the proposed 3D phase-encoded eddy current measurements. This work only considered the first 40 ms of the diffusion gradient-induced eddy current measurement data for voxel selection and subsequent processing. Readout durations of 26 ms (spiral) and 32 ms (EPI) could therefore be adequately corrected for. In case the signal decay is a limiting factor, a split acquisition approach with the excitation after the diffusion gradients, as proposed for GIRF measurements by Scholten et al., could be adopted.⁵⁷ Lowering the acquisition BW of the eddy current measurement

is likely to only provide limited improvements. Despite the need for dedicated hardware, the use of field probes could offer sufficient SNR for determining higher-order basis functions.²⁸

The proposed framework is not limited to characterization and correction of eddy currents induced by second-order MC SE-cDTI diffusion-encoding waveforms, and can be adapted to study eddy currents arising from, for example, zeroth- or first-order MC diffusion-encoding waveforms.

Although this work showed the feasibility of characterizing and correcting for zeroth- and first-order diffusion gradient-induced eddy currents, further efforts are necessary to simplify and shorten the characterization step. Currently, the protocol takes approximately 11 min per diffusion direction for a $7 \times 7 \times 7$ acquisition grid. Using smaller grid sizes increases the sensitivity to intravoxel dephasing in the presence of B_0 field gradients in the spherical phantom. Instead of scanning with a finer acquisition grid, interpolating the existing $7 \times 7 \times 7$ to higher resolutions might offer improvements. Because the gradient system will heat up during the course of the scan, temperature-dependent effects, which are known to influence GIRFs^{31,58}, might also have affected the eddy current characterization. Accounting for this temperature dependence, one could further examine if the determined diffusion gradient-induced eddy current coefficients exhibit similar temporal stability as GIRFs.²³

Theoretically, a GIRF could offer an ideal all-in-one solution to predict the entire gradient waveform response.

However, to design a chirp waveform that can exhibit sufficient gradient amplitude and slew rate to characterize the full frequency range of second-order MC diffusion gradients (see Supporting Information Figure S1 and Supporting Information Text S9: Computation of diffusion-encoding gradient power spectrum), whilst minimizing intravoxel phase dispersion and waveform duration remains challenging. Moreover, the diffusion gradient-induced eddy current responses were shown to be nonlinear in gradient amplitude and could not be described by a linear model (i.e., > 3 singular values were above the noise floor).

The use of a 2D RF pulse to reduce the excited FOV limits the SNR improvement available from interleaved slice imaging, as is common in motion-compensated SE imaging.^{1,2,12}

In our work, we characterized 9 diffusion directions fixed to the scanner gradient system axes at 2 b values. Characterizing multiple diffusion directions at once would offer flexibility to adapt scan protocols without the need for additional eddy current measurements.

Although approaches have been proposed to null zeroth-order eddy currents using diffusion gradient waveform optimization,^{59,60} the inability to address spatially dependent (first- or higher order) eddy currents would be noticeable when imaging at offcenter locations commonly required for imaging the in vivo heart. By characterizing the diffusion gradient-induced eddy currents, these could be used as an input to sequence optimization tools to compute diffusion gradient waveforms in real time, which are inherently compensated for zeroth-, first-, and/or higher order eddy currents to image double-oblique slices at arbitrary orientations.

6 | CONCLUSION


In this work, we characterized eddy current phase accrual caused by the diffusion gradient waveforms for both echo-planar and spiral cDTI. It was found that diffusion gradient-induced eddy currents violate the linear system assumption and therefore need to be measured separately to a GIRF to be used during image reconstruction. Zeroth- and first-order correction was found to provide an adequate degree of correction on phantom, ex vivo, and in vivo data, paving the way for distortion-free second-order MC-SE cDTI protocols.


ACKNOWLEDGMENT


Open access funding provided by Eidgenössische Technische Hochschule Zurich.

ORCID

Robbert J. H. van Gorkum  <https://orcid.org/0000-0003-1072-0477>

Christian Guenther  <https://orcid.org/0000-0001-8707-7016>

Christian T. Stoeck  <https://orcid.org/0000-0001-8670-0929>

Sebastian Kozerke  <https://orcid.org/0000-0003-3725-8884>

TWITTER

Sebastian Kozerke  @CMR_Zurich

REFERENCES

- Gotschy A, von Deuster C, Weber L, et al. CMR diffusion tensor imaging provides novel imaging markers of adverse myocardial remodeling in aortic stenosis. *JACC Cardiovasc Imaging* 2021;14:1472-1474.
- Gotschy A, von Deuster C, van Gorkum RJH, et al. Characterizing cardiac involvement in amyloidosis using cardiovascular magnetic resonance diffusion tensor imaging. *J Cardiovasc Magn Reson* 2019;21:56.
- Nielles-Vallespin S, Khaliq Z, Ferreira PF, et al. Assessment of myocardial microstructural dynamics by in vivo diffusion tensor cardiac magnetic resonance. *J Am Coll Cardiol* 2017;69:661-676.
- von Deuster C, Sammut E, Asner L, et al. Studying dynamic Myofiber aggregate reorientation in dilated cardiomyopathy using in vivo magnetic resonance diffusion tensor imaging. *Circ Cardiovasc Imaging* 2016;9:e005018.
- Khaliq Z, Ferreira PF, Scott AD, et al. Diffusion tensor cardiovascular magnetic resonance in cardiac amyloidosis. *Circ Cardiovasc Imaging* 2020;13:1-11.
- Khaliq Z, Ferreira PF, Scott AD, et al. Deranged myocyte microstructure in situs Inversus Totalis demonstrated by diffusion tensor cardiac magnetic resonance. *JACC Cardiovasc Imaging* 2018;11:1360-1362.
- Mekkaoui C, Huang S, Chen HH, et al. Fiber architecture in remodeled myocardium revealed with a quantitative diffusion CMR tractography framework and histological validation. *J Cardiovasc Magn Reson* 2012;14:70.
- von Deuster C, Stoeck CT, Genet M, Atkinson D, Kozerke S. Spin echo versus stimulated echo diffusion tensor imaging of the in vivo human heart. *Magn Reson Med*. 2016;76:862-872.
- Scott AD, Nielles-Vallespin S, Ferreira PF, et al. An in-vivo comparison of stimulated-echo and motion compensated spin-echo sequences for 3 T diffusion tensor cardiovascular magnetic resonance at multiple cardiac phases. *J Cardiovasc Magn Reson*. 2018;20:1-15.
- Dou J, Reese TG, Tseng W-YI, Wedeen VJ. Cardiac diffusion MRI without motion effects. *Magn Reson Med*. 2002;48:105-114.
- Tseng W-YI, Reese TG, Weisskoff RM, Wedeen VJ. Cardiac diffusion tensor MRI in vivo without strain correction. *Magn Reson Med*. 1999;42:393-403.
- Stoeck CT, von Deuster C, Genet M, Atkinson D, Kozerke S. Second-order motion-compensated spin echo diffusion tensor imaging of the human heart. *Magn Reson Med*. 2016;75:1669-1676.

13. Welsh CL, DiBella EVR, Hsu EW. Higher-order motion-compensation for in vivo cardiac diffusion tensor imaging in rats. *IEEE Trans Med Imaging*. 2015;34:1843-1853.
14. Nguyen C, Fan Z, Sharif B, et al. In vivo three-dimensional high resolution cardiac diffusion-weighted MRI : a motion compensated diffusion-prepared balanced steady-state free precession approach. *Magn Reson Med* 2014;72:1257-1267.
15. Chan RW, von Deuster C, Giese D, et al. Characterization and correction of eddy-current artifacts in unipolar and bipolar diffusion sequences using magnetic field monitoring. *J Magn Reson* 2014;244:74-84.
16. Gorodetzky M, Ferreira PF, Nielles-Vallespin S, et al. High resolution in-vivo DT-CMR using an interleaved variable density spiral STEAM sequence. *Magn Reson Med* 2019;81:1580-1594.
17. Gorodetzky M, Scott AD, Ferreira PF, Nielles-Vallespin S, Pennell DJ, Firmin DN. Diffusion tensor cardiovascular magnetic resonance with a spiral trajectory: an in vivo comparison of echo planar and spiral stimulated echo sequences. *Magn Reson Med*. 2018;80:648-654.
18. Sutton BP, Noll DC, Fessler JA. Fast, iterative image reconstruction for MRI in the presence of field inhomogeneities. *IEEE Trans Med Imaging*. 2003;22:178-188.
19. Lee Y, Wilm BJ, Brunner DO, et al. On the signal-to-noise ratio benefit of spiral acquisition in diffusion MRI. *Magn Reson Med* 2021;85:1924-1937.
20. Andersson JLR, Hutton C, Ashburner J, Turner R, Friston K. Modeling geometric deformations in EPI time series. *Neuroimage*. 2001;13:903-919.
21. Man LC, Pauly JM, Macovski A. Improved automatic off-resonance correction without a field map in spiral imaging. *Magn Reson Med*. 1997;37:906-913.
22. Noll DC, Meyer CH, Pauly JM, Nishimura DG, Macovski A. A homogeneity correction method for magnetic resonance imaging with time-varying gradients. *IEEE Trans Med Imaging*. 1991;10:629-637.
23. Vannesjo SJ, Graedel NN, Kasper L, et al. Image reconstruction using a gradient impulse response model for trajectory prediction. *Magn Reson Med* 2016;76:45-58.
24. Wilm BJ, Barmet C, Pavan M, Pruessmann KP. Higher order reconstruction for MRI in the presence of spatiotemporal field perturbations. *Magn Reson Med*. 2011;65:1690-1701.
25. King KF, Ganin A, Zhou XJ, Bernstein MA. Concomitant gradient field effects in spiral scans. *Magn Reson Med*. 1999;41:103-112.
26. Du YP, Joe Zhou X, Bernstein MA. Correction of concomitant magnetic field-induced image artifacts in nonaxial echo-planar imaging. *Magn Reson Med*. 2002;48:509-515.
27. Barmet C, De Zanche N, Wilm BJ, Pruessmann KP. A transmit/receive system for magnetic field monitoring of in vivo MRI. *Magn Reson Med*. 2009;62:269-276.
28. Gross S, Vionnet L, Kasper L, Dietrich BE, Pruessmann KP. Physiology recording with magnetic field probes for fMRI denoising. *Neuroimage*. 2017;154:106-114.
29. Vannesjo SJ, Haeblerlin M, Kasper L, et al. Gradient system characterization by impulse response measurements with a dynamic field camera. *Magn Reson Med* 2013;69:583-593.
30. Rahmer J, Mazurkewitz P, Börnert P, Nielsen T. Rapid acquisition of the 3D MRI gradient impulse response function using a simple phantom measurement. *Magn Reson Med*. 2019;82:2146-2159.
31. Nussbaum J, Dietrich BE, Wilm BJ, Pruessmann KP. Thermal variation in gradient response: measurement and modeling. *Magn Reson Med*. 2022;87:2224-2238.
32. Bernstein MA, Zhou XJ, Polzin JA, et al. Concomitant gradient terms in phase contrast MR: analysis and correction. *Magn Reson Med* 1998;39:300-308.
33. Norris DG, Hutchison JMS. Concomitant magnetic field gradients and their effects on imaging at low magnetic field strengths. *Magn Reson Imaging*. 1990;8:33-37.
34. Brodsky EK, Klaers JL, Samsonov AA, Kijowski R, Block WF. Rapid measurement and correction of phase errors from B0 eddy currents: impact on image quality for non-Cartesian imaging. *Magn Reson Med*. 2013;69:509-515.
35. Wilm BJ, Barmet C, Pruessmann KP. Fast higher-order MR image reconstruction using singular-vector separation. *IEEE Trans Med Imaging*. 2012;31:1396-1403.
36. Halko N, Martinsson PG, Tropp JA. Finding structure with randomness: probabilistic algorithms for constructing approximate matrix decompositions. *SIAM Rev*. 2011;53:217-288.
37. Oh CH, Hilal SK, Cho ZH. Selective partial inversion recovery (SPIR) in steady state for selective saturation magnetic resonance imaging (MRI). In: Book of Abstracts: Seventh Annual Meeting of the Society of Magnetic Resonance in Medicine, Vol 2, San Francisco, CA, 1988. p. 1042.
38. Kaldoudi E, Williams SCR, Barker GJ, Tofts PS. A chemical shift selective inversion recovery sequence for fat-suppressed MRI: theory and experimental validation. *Magn Reson Imaging*. 1993;11:341-355.
39. Feinberg DA, Hoenninger JC, Crooks LE, Kaufman L, Watts JC, Arakawa M. Inner volume MR imaging: technical concepts and their application. *Radiology*. 1985;156:743-747.
40. Nguyen C, Fan Z, Xie Y, et al. In vivo contrast free chronic myocardial infarction characterization using diffusion-weighted cardiovascular magnetic resonance. *J Cardiovasc Magn Reson* 2014;16:68.
41. Meyer CH, Pauly JM, Macovski A, Nishimura DG. Simultaneous spatial and spectral selective excitation. *Magn Reson Med*. 1990;15:287-304.
42. Nehrke K, Börnert P, Groen J, Smink J, Böck JC. On the performance and accuracy of 2D navigator pulses. *Magn Reson Imaging*. 1999;17:1173-1181.
43. Jezzard P, Barnett AS, Pierpaoli C. Characterization of and correction for eddy current artifacts in echo planar diffusion imaging. *Magn Reson Med*. 1998;39:801-812.
44. Stimm J, Buoso S, Berberoğlu E, Kozerke S, Genet M, Stoeck CT. A 3D personalized cardiac myocyte aggregate orientation model using MRI data-driven low-rank basis functions. *Med Image Anal*. 2021;71:102064.
45. Otsu N. A threshold selection method from gray-level histograms. *IEEE Trans Syst Man Cybern*. 1979;9:62-66.
46. Funai AK, Fessler JA, Yeo DTB, Olafsson VT, Noll DC. Regularized field map estimation in MRI. *IEEE Trans Med Imaging*. 2008;27:1484-1494.
47. van Gorkum RJH, von Deuster C, Guenther C, Stoeck CT, Kozerke S. Analysis and correction of off-resonance artifacts in echo-planar cardiac diffusion tensor imaging. *Magn Reson Med*. 2020;84:2561-2576.

48. Buehrer M, Pruessmann KP, Boesiger P, Kozerke S. Array compression for MRI with large coil arrays. *Magn Reson Med.* 2007;57:1131-1139.
49. Pruessmann KP, Weiger M, Börner P, Boesiger P. Advances in sensitivity encoding with arbitrary k-space trajectories. *Magn Reson Med.* 2001;46:638-651.
50. Vishnevskiy V, Gass T, Szekely G, Tanner C, Goksel O. Isotropic total variation regularization of displacements in parametric image registration. *IEEE Trans Med Imaging.* 2017;36:385-395.
51. Basser PJ, Mattiello J, LeBihan D. MR diffusion tensor spectroscopy and imaging. *Biophys J.* 1994;66:259-267.
52. Ferreira P, Kilner PJ, McGill L, et al. Aberrant myocardial sheetlet mobility in hypertrophic cardiomyopathy detected using in vivo cardiovascular magnetic resonance diffusion tensor imaging. *J Cardiovasc Magn Res.* 2014; 16(Suppl 1):P338.
53. Stoeck CT, von Deuster C, Fleischmann T, Lipiski M, Cesarovic N, Kozerke S. Direct comparison of in vivo versus postmortem second-order motion-compensated cardiac diffusion tensor imaging. *Magn Reson Med.* 2018;79: 2265-2276.
54. Stoeck CT, von Deuster C, van Gorkum RJH, Kozerke S. Motion and eddy current-induced signal dephasing in in vivo cardiac DTI. *Magn Reson Med.* 2020;84:277-288.
55. Scott AD, Nielles-Vallespin S, Ferreira PF, McGill L-A, Pennell DJ, Firmin DN. The effects of noise in cardiac diffusion tensor imaging and the benefits of averaging complex data. *NMR Biomed.* 2016;29:588-599.
56. Jones DK, Basser PJ. "Squashing peanuts and smashing pumpkins": how noise distorts diffusion-weighted MR data. *Magn Reson Med.* 2004;52:979-993.
57. Scholten H, Stich M, Köstler H. Phantom-based high-resolution measurement of the gradient system transfer function. In Proceedings of the 29th Annual Meeting of the ISMRM, Virtual Conference, 2021. p. 6.
58. Busch J, Vannesjo SJ, Barmet C, Pruessmann KP, Kozerke S. Analysis of temperature dependence of background phase errors in phase-contrast cardiovascular magnetic resonance. *J Cardiovasc Magn Reson.* 2014;16:97.
59. Yang G, McNab JA. Eddy current nulled constrained optimization of isotropic diffusion encoding gradient waveforms. *Magn Reson Med.* 2019;81:1818-1832.
60. Aliotta E, Moulin K, Ennis DB. Eddy current-nulled convex optimized diffusion encoding (EN-CODE) for distortion-free diffusion tensor imaging with short echo times. *Magn Reson Med.* 2018;79:663-672.

SUPPORTING INFORMATION

Additional supporting information may be found in the online version of the article at the publisher's website.

Figure S1: Gradient impulse response functions with the diffusion gradient spectrum of a second-order motion-compensated gradient. Magnitude of self-terms for the X, Y, and Z gradient coils are shown. Note the dedicated y-axis for the diffusion gradient spectrum

Figure S2: Forward model simulation of a 2D RF excitation beam. (Top-left) Effective out-in Archimedean spiral

waveforms. (Top-right) Hanning-window filtered RF envelope. (Bottom-left) Bloch-simulated 3D RF beam profile. (Bottom-right) A cross-section of the beam profile amplitude along $x = 0$ mm is plotted

Figure S3: Schematic overview of the data processing of the diffusion gradient-induced eddy current data

Figure S4: Example in vivo field map. (Left) The magnitude image of the data acquired at the first TE, (Right) the corresponding prepared field map is shown with the left-ventricular contour overlaid (dashed white lines)

Figure S5: Overview of all zeroth- and first-order diffusion gradient-induced eddy current coefficients plotted for 9 directions as given in Table S1. Solid colored lines indicate $b = 150$ s/mm² data and dashed colored lines indicate $b = 450$ s/mm² data. The dashed black line marks the echo time

Figure S6: Singular value decomposition (SVD) analysis of the zeroth- and first-order diffusion gradient-induced eddy currents (EC) for 9 diffusion directions acquired with b values 150 s/mm² and 450 s/mm². SVD components are plotted in SNR units. Inset figures highlight SVD component range from 3 to 9. The dashed black line marks the noise floor (SNR = 1)

Figure S7: Histograms comparing LV ROI ex vivo data seen in Figure 7 for the reference (blue) and proposed (orange) reconstruction approaches for both EPI and spiral readouts. HA, helix angle; TA, transverse angle; E2A, absolute sheetlet angle; MD, mean diffusivity; FA, fractional anisotropy

Figure S8: EPI and spiral in vivo diffusion-weighted images of the 12 diffusion directions are shown for the reference and proposed reconstruction approaches and their respective normalized absolute difference. Diffusion directions 1–3 were acquired with a b value of 150 s/mm², and directions 4–12 were acquired with a b value of 450 s/mm². The red arrow indicates the phase encode direction for EPI. The white arrow highlights a left-ventricular/liver section. Diffusion weighted images are normalized for display purposes only

Figure S9: Histograms comparing in vivo LV ROI cDTI data seen in Figure 9 for the reference (blue) and the proposed (orange) reconstructions for both EPI and spiral readouts. HA, helix angle; TA, transverse angle; E2A, absolute sheetlet angle; MD, mean diffusivity; FA, fractional anisotropy

Figure S10: Overview of the in vivo SNR. Using the mean SNR in the left-ventricular region of interest, the mean and standard deviation across all volunteers was computed per diffusion direction and are displayed for spiral (SPI) and EPI. Note the influence of the diffusion-weighting on the SNR

Table S1: Diffusion gradient directions used during the study

Table S2: Diffusion gradient directions characterized for the in vivo study with their corresponding b value

Text S1: GIRF acquisition and processing

Text S2: Dynamic δf_0 stabilization

Text S3: 2D RF excitation beam simulation

Text S4: Diffusion directions

Text S5: Diffusion gradient-induced eddy current data processing

Text S6: Ex vivo heart preparation

Text S7: Heartrate correction

Text S8: Eddy current analysis noise signal

Text S9: Computation of diffusion encoding gradient power spectrum

How to cite this article: van Gorkum RJH, Guenthner C, Koethe A, Stoeck CT, Kozerke S. Characterization and correction of diffusion gradient-induced eddy currents in second-order motion-compensated echo-planar and spiral cardiac DTI. *Magn Reson Med.* 2022;88:2378-2394. doi: 10.1002/mrm.29378